Supplementary Information

Ultrafast Synthesis of Efficient Urea Oxidation Electrocatalyst for Urea-Assisted Fast-Charging Zn-Air Battery and Water Splitting

Tongtong Li[1, 6], Zhiyang Zheng[1, 6], Zherui Chen[3], Mengtian Zhang[1], Zhexuan Liu[1], Huang Chen[1], Xiao Xiao[1], Shaogang Wang[4], Haotian Qu[1], Qingjin Fu[1], Le Liu[1], Ming Zhou[5], Boran Wang[2]*, Guangmin Zhou[1]*

[1] Institute of Materials Research, Tsinghua Shenzhen International Graduate School, Tsinghua University, Shenzhen 518055, P. R. China.

[2] Guangxi Key Laboratory of Electrochemical Energy Materials, School of Chemistry and Chemical Engineering Guangxi University Nanning 530004, PR. China

[3] Future Technology School, Shenzhen Technology University, Shenzhen 518118, PR China

[4] Shenyang National Laboratory for Materials Science, Institute of Metal Research, Chinese Academy of Sciences, Shenyang 110016, P. R. China.

[5] School of New Energy and Materials and State Key Laboratory of Oil and Gas Reservoir Geology and Exploitation Engineering, Southwest Petroleum University, Chengdu, Sichuan, 610500 China

[6] These authors contributed equally: Tongtong Li, Zhiyang Zheng

e-mail: wangbr@gxu.edu.cn; guangminzhou@sz.tsinghua.edu.cn

Methods

Materials and chemicals

Potassium hydroxide (KOH, 95%), Iron (III) nitrate nonahydrate ($Fe(NO_3)_3·9H_2O$, 98-101%), sodium thiosulfate pentahydrate ($Na_2S_2O_3·5H_2O$), urea ($CO(NH_2)_2$, 99.5%) were acquired from Macklin. Hydrochloric acid (HCl), ethanol (C_2H_5OH), ferrous sulfate heptahydrate ($FeSO_4·7H_2O$) nickel(II) nitrate hexahydrate ($Ni(NO_3)_2·6H_2O$ were acquired from Aladdin. The Nafion solution (5%), and RuO_2 (with a Ru content >75%) were purchased from Suzhou Sinero Technology Co., LTD. The nickel foam (NF) used in this work has a thickness of 1.0 mm and is obtained from Shanghai Tankii Alloy Material Co., Ltd. NF has been cleaned sequentially with 1.0 M HCl, ethanol, and deionized water (DI water) before being used. DI water was used in all experimental sections, having a resistance of 18.25 MΩ cm. Titanium-supported IrO_2 electrode was purchased by Suzhou Shuertai Industrial Technology Co., Ltd.

Synthesis of S-NiFe-LDH catalyst on Ni foam

The S-NiFe-LDH catalysts were prepared on Ni foam by a one-step solution-phase method at room temperature. The solution was prepared by dissolving 2 M $Fe(NO_3)_3·9H_2O$ and 0.5 M $Na_2S_2O_3·5H_2O$ into 10 mL DI water in a small bottle, and then one piece of Ni foam (1 × 2 cm^2, thickness: 1.0 mm; aperture: 0.1 mm; porosity: 97.2%) was placed into the solution. After 2 seconds, the color of the NF was changed from its original metal luster and became black. Then, the obtained S-NiFe-LDH was washed with DI water and ethanol. In this method, Ni foam serves as both the substrate and the Ni source; $Fe(NO_3)_3·9H_2O$ is the Fe source; and $Na_2S_2O_3·5H_2O$ serves as the S source and also plays a crucial role in accelerating the whole reaction. Ni can react with Fe^{3+} in an aqueous solution ($Ni + 2Fe^{3+} \rightarrow Ni^{2+} + 2Fe^{2+}$), but the reaction is very slow and requires high temperature. $Na_2S_2O_3·5H_2O$ dissolves in water very quickly and generates a weakly alkaline solution. With its addition, Ni^{2+} and Fe^{2+} rapidly combined with OH^- and simultaneously reacted

with the dissolved oxygen to produce the (Ni, Fe)OOH layer. Subsequently, the thiosulfate ions further reacted with the (Ni, Fe)OOH and finally generated a dense and S-doped (Ni, Fe)OOH layer in situ.

Synthesis of NiFe-LDH catalyst

The electrodeposition of NiFe-LDH is carried out in a three-electrode system. The as-prepared NF, a Pt net, and a saturated calomel electrode are used as the working, counter, and reference electrodes, respectively. The aqueous electrochemical bath consisted of $Ni(NO_3)_2 \cdot 6H_2O$ (15 mM) and $FeSO_4 \cdot 7H_2O$ (15 mM) with a continuous N_2 flow. The applied potential of –1.0 V (*vs.* saturated calomel electrode, SCE) was used in the electrochemical workstation program during the electrodeposition process, with samples obtained after 120 seconds. The sample was subsequently washed with deionized water and dried in air.

Synthesis of RuO_2/NF

20 mg of 20 wt% RuO_2 powder, 500 μL of ethanol, and 150 μL of Nafion were sonicated for 30 minutes. Next, 100 μL of the above dispersion solution was slowly dropped on cleaned NF (10 × 10 mm^2) and dried in air for 10 h to prepare the RuO_2/NF electrode.

Material Characterizations

Scanning electron microscope (SEM) images were obtained by HITACHI SU8010. TEM images were characterized by FEI TalosF200S G2 at 200 kV. XRD patterns were obtained by Bruker D8 Advance at a rate of 5° min^{-1}. XPS patterns were performed on an Escalab Xi + system. Raman spectra were performed on a Renishaw inVia. The water contact angle was measured by using a contact angle goniometer (OCA 20, Dataphysics). The contact angle of the gas bubble in the electrolyte was measured using the Lauda Scientific LSA100 instrument via the captive-bubble method controlled bubble volume to 5 μL. The optical images of gas bubbles were recorded by a high-speed CCD camera (1-6010, NAVITAR). The thickness of the samples and roughness were concluded by atomic force microscopy (AFM) with SPI 3800N probe station (Seiko, Japan). The X-ray tomography tests were performed on an Xradia Versa XRM-500 system. 1600 projections were recorded while the sample was rotated about 360°. The pixel size of the reconstructed 3D image is about 1.09 μm. The 3D data was processed and visualized using Avizo Fire software.

Electrochemical test

All electrochemical experiments were performed on an electrochemical workstation (CHI 660E, CH Instruments, Inc.). All mentioned potentials of UOR, HER, and OER were converted to potentials relative to reversible hydrogen electrode (RHE) according to $E_{vs.\ RHE} = E_{vs.\ Hg/HgO} + 0.059 \times pH + 0.098$ V. The electrolytes involved in this work include 1 M KOH and 1 M KOH with 0.33 M urea. Linear sweep voltammetry (LSV) curves were measured at a scan rate of 5 mV s^{-1} (with *iR* compensation). The as-fabricated electrodes (1×1 cm^2) were clamped to make an electrochemical test. The resistance was determined by constant potential electrochemical impedance spectroscopy (EIS) at an amplitude of 5 mV over a frequency range of 10^6 to 0.01 Hz (excluding operando EIS). Bode plots were at an amplitude of 5 mV over a frequency range of 10^6 to 0.1 Hz. The CV was tested with different scan rates (20, 40, 60, 80, and 100 mV s^{-1}) from 76 to 176 mV (*vs*. RHE) to calculate the effective ECSA of the catalyst. A linear plot was obtained by plotting the value of Δj ($|j_{max} - j_{min}|/2$) of the current density against the CV scan rate. The slope of the fitted line is C_{dl}, which is proportional to the electrochemical surface area. Tafel slopes were calculated according to

the Tafel equation: $\eta = a + b * log\, j$, where η is potential, a is the Tafel constant, b is the Tafel slope, and j is the current density. All experiments were carried out at room temperature. The electricity expense of hydrogen production in the two-electrode water-splitting system was calculated by the equation:

$$W_{H2} = \frac{IUT}{Q_{H_2} \times 10^3} \quad (1)$$

where W_{H_2} (kWh m^{-3}) represents the direct electricity consumption, I (A) and U (V) are the direct current and voltage of the two-electrode system, respectively, Q represents the hydrogen production during the detection period, and T is detection time.

The actual electricity expense for electrolyzing water was calculated by the equation:

$$W = QU = 2 \times 6.023 \times 10^{23} \times 1.6 \times 10^{-19} \times \mathrm{EOP} \quad (2)$$

where EOP represents the actual operating voltage for electrolyzing water in a two-electrode electrolyzer.

Half-cell UOR test

The experimental setup employed a Hg/HgO electrode as the reference electrode, a graphite rod (Gaossunion) as the counter electrode, and the prepared sample as the working electrode. UOR test electrolyte was 1 M KOH with 0.33 M urea. Stability tests were carried out by using the chronopotentiometry program at 100 mA cm^{-2}. EIS tests were performed at a potential of 400 mV (*vs.* RHE).

Full cell (alkaline-alkaline UOR/HER cell) test

The electrolyte consisted of 1 M KOH with 0.33 M urea. The stability test was conducted using a chronopotentiometry (CP) procedure, maintaining a current density of 100 mA cm^{-2}, with the electrolyte being refreshed every 24 hours.

Assembling and performance test of the urea-assisted rechargeable Zn-air battery (UAZAB)

The performance and stability of the aqueous zinc-air battery were evaluated using a custom-built ZAB system, with electrochemical measurements conducted on a Neware battery test system (CT-4008T) at room temperature. The UAZAB was assembled in a layered configuration starting with securing the charging-side catalyst (S-NiFe-LDH) onto the anode-side base plate using iron wires, ensuring the catalyst was suspended within the inner groove of the plate. A gasket (Gasket 1) was then placed on the first base plate, followed by the installation of an anion exchange membrane. A second gasket (Gasket 2) was added, and the second base plate was positioned above it. A zinc plate anode was fixed onto the second base plate using iron wires. Subsequently, a third gasket (Gasket 3) was placed on the second base plate, and the discharging-side catalyst (2.0 mg/cm^2 Pt/C) was deposited onto the gasket. Finally, a piece of rolled nickel foam was placed on top of the catalyst, and the third base plate was installed to complete the assembly, resulting in the final UAZAB device. The battery employed a dual-electrolyte configuration to optimize the performance of both the charging and discharging processes. Charging Side Electrolyte: The charging side utilized an electrolyte consisting of 1 M KOH with 0.33 M urea, which was stored in a 100 mL reservoir and continuously circulated at a flow rate of ~8 mL min^{-1}. Discharging Side Electrolyte: The discharging side employed an electrolyte composed of 6 M KOH and 0.2 M $Zn(Ac)_2$, which was also circulated at a flow rate of ~8 mL min^{-1}. The air electrode was directly exposed to ambient air to facilitate oxygen diffusion for the oxygen reduction reaction (ORR). The cell design featured a chamber

volume of 7.07 mL to accommodate the electrolyte, with the exposed electrode area controlled by the template hole dimensions. Zinc plates with a thickness of 2.0 mm and a reactive surface area of 7.07 cm^2 were employed as the anode for rate capability and cycling stability tests.

In-situ TIR Sensor System Setup

A custom in situ Total Internal Reflection (TIR) apparatus has been engineered to monitor the progression of the initial electrode potential shift during the oxygen evolution reaction. This in-situ TIR apparatus encompasses an illumination setup, an electrochemical setup, and a detection module. The electrochemical setup is composed of a reference electrode (a mercury/mercury oxide electrode), a counter electrode (a graphite electrode), a working electrode, an electrolyte solution (1 M potassium hydroxide combined with 0.33 M urea), and a specially designed electrolytic cell. The working electrode is designed with a sample and a copper plate to ensure a tight interface between the sample and the prism. The visualization system is equipped with a Charge Coupled Device (CCD) camera (Retiga R3, Qimaging, Canada) and an optical lens (provided by Guangzhou ZhiSai Electronic Technology Co, LTD, China). In the illumination setup, the red light emitted from a light-emitting diode (LED) is gathered by a 25x objective lens (GCO-2104, Daheng Optics, China), and subsequently concentrated onto an aperture with a 0.3 mm diameter. The light emanating from this aperture is then directed through a double achromatic lens (GCL-010650, Daheng Optoelectronics) to form a collimated beam of parallel light. This incident light, with a wavelength of 632.8 nm, is refined by a bandpass filter (FL632.8-10, Thorlabs, USA) to minimize stray light, and further processed by a linear polarizer (GCL-050003, Daheng Optics, China, with an extraction ratio of 500:1). By adjusting the aperture and focal length of the detection module's imaging lens, the CCD camera captures the outgoing light, resulting in a series of images depicting the surface of the hydrogen evolution catalytic electrode.

An electrochemical workstation facilitates the testing of the electrochemical setup. A linear sweep voltammetry (LSV) test is initiated, with the voltage range scanned from 1.3 to 1.6 V (*vs.* RHE), at a scanning rate of 1 mV per second, and the test is conducted with automatic iR compensation. For the CCD camera settings, the exposure time is set to 6 milliseconds, with an acquisition interval of 1 second. Synchronization between the electrochemical test and optical detection is initiated upon the commencement of the LSV scanning by the electrochemical workstation. As the potential escalates during the LSV test, the equivalent refractive index of the electrolyte within the detection depth of the electrode surface diminishes due to the formation of N_2 and CO_2 microbubbles, which in turn increases the intensity of the reflected light. The distribution of the onset potential is derived by analyzing how the light intensity at each detection point on the electrode surface responds to potential changes. Given the significant refractive index contrast between the N_2 and CO_2 bubbles and the electrolyte, the emergence of N_2 and CO_2 bubbles will result in a decrease in the equivalent refractive index of the electrolyte within the detection depth. Consequently, a sparse presence of bubbles on the electrode surface will notably reduce reflectivity. When the initial light intensity undergoes a change of one-thousandth, the corresponding potential value is identified as the initial potential determined through the total internal reflection imaging technique. It should be noted that bubble formation precedes the initial potential, ensuring that the impact of bubbles on the prism does not compromise the test outcomes.

Theoretical simulation

The calculations were performed using the CP2K software package,[1, 2] employing the Perdew-

Burke-Ernzerhof (PBE)[3] exchange-correlation functional. A double zeta valence polarized with short-range Gaussian type orbitals (DZVP) basis set was used, along with the Goedecker-Teter-Hutter (GTH) pseudopotentials. Structural periodicity was applied in the XY directions with non-periodic boundary conditions along the Z direction for a model of initial dimensions 10.539 Å × 12.17 Å. All calculations were for the (001) surface of LDH. The plane-wave cutoff energy was set to 350 Ry (1 Ry = 13.6056923 eV). Self-consistent field (SCF) calculations were performed with a density matrix convergence criterion of 1.0×10^{-6}.[4] The Brillouin zone was sampled at the Gamma point, and the orbital transformation (OT) method was employed for the electronic structure optimization. For Ni atoms, the DFT+U approach was applied with a U value of 2 eV. Dispersion interactions were corrected using the DFT-D3 method.[5]

The calculation of adsorption energy is completed by the following equation：

$$\triangle E = E - E_{LDH} - E_C \quad (3)$$

Where E is the total energy after the adsorption and stabilization of LDH with urea or carbon dioxide, E_{LDH} is the energy of LDH, and EC is the energy of urea or carbon dioxide.

In situ Attenuated Total Reflectance Infrared spectroscopy measurement

The surface-enhanced infrared absorption spectroscopy (SEIRAS) with the attenuated total reflection (ATR) configuration was employed. A Thermo Nicolet 6700 spectrometer equipped with a mercury cadmium telluride (MCT) detector, cooled by liquid nitrogen, was employed for the electrochemical attenuated total reflectance-surface enhanced infrared absorption spectroscopy (ATR-SEIRAS) measurements. Chemical deposition of Au thin film (~60 nm) on the Si prism was prepared according to a "two-step wet process". Before the chemical deposition of Au, the Si prism surface for IR reflection was polished with Diamond suspension and cleaned in water with sonication. Then the prism was soaked in a piranha solution (7:3 volumetric ratio of 98% H_2SO_4 and 30% H_2O_2) for 2 hours. 30 ul ink was deposited and dried on the Au-film working electrode, then the ink-coated prism was assembled into a homemade spectroelectrochemical cell as the working electrode, Hg/HgO was used as a reference, which was introduced near the working electrode via a Luggin capillary, a Pt mesh (1 cm × 1 cm) was serving as the counter electrode. All spectra were shown in $\frac{\Delta R}{R} = \frac{E_S - E_R}{E_R}$, with *Es* and E_R representing the sample and reference spectra, respectively. Each infrared absorption spectrum was acquired by averaging 128 scans at a resolution of 8 cm^{-1}. All the infrared spectra were obtained after a constant potential was applied to the catalyst's electrode for 5 min.

COMSOL simulations

Utilizing the finite element method, we employed COMSOL Multiphysics 6.2 to simulate the process of bubble evolution and the resultant stress exerted on the anode. The primary control equations governing this simulation are outlined below:

The bubble evolution can be described using a volume of fluid (VF) with two-phase flow, the VF fractions (α, $0\leq\alpha\leq1$) representing the gas phase (VF1) and an electrolyte phase (VF2) in this model. It denotes that the cell is full of the gas phase and electrolyte phase if the α=1 and α=0, respectively. Based on α in this model, the variable and tracking of the interfaces between the phases will be calculated in each control volume. Therefore, the phase field equation is the following Equations (4) and (5).

$$\frac{\partial \phi}{\partial t} + \boldsymbol{\mu} \cdot \nabla \phi = \nabla \cdot \frac{\gamma \lambda}{\varepsilon_{\mathrm{pf}}^2} \nabla \psi \tag{4}$$

$$\psi = -\nabla \cdot \varepsilon_{\mathrm{pf}}^2 \nabla \phi + (\phi^2 - 1)\phi + \frac{\varepsilon_{\mathrm{pf}}^2}{\lambda} \frac{\partial f}{\partial \phi} \tag{5}$$

where ϕ is the phase variable, $\boldsymbol{\mu}$ is the fluid flow velocity vector, ε_{pf} is the interface thickness control parameter, ψ is the intermediate variable in the phase field, λ is $3\varepsilon_{pf}\sigma/\sqrt{8}$, γ is $\chi\varepsilon_{\mathrm{pf}}^2$, χ is the migration mobility adjustment parameter, $\nabla\psi$ is the gradient of the external free energy, σ is the surface tension, and t is time.

The Navier-Stokes Equations (6) and (7) describe the incompressible flow.

$$\nabla \cdot \vec{\mu} = 0 \tag{6}$$

$$\rho\left(\frac{\partial \vec{\mu}}{\partial t} + \vec{\mu} \cdot \nabla \vec{\mu}\right) = -\nabla p + \mu \nabla^2 \vec{\mu} + \rho \vec{g} + \overrightarrow{F_{st}} \tag{7}$$

Where p is the pressure, ρ is the density of the electrolyte, g is the gravitational acceleration, and F_{st} the surface tension.

Fig. S1 The photograph of S-NiFe-LDH electrodes prepared in 2 seconds.

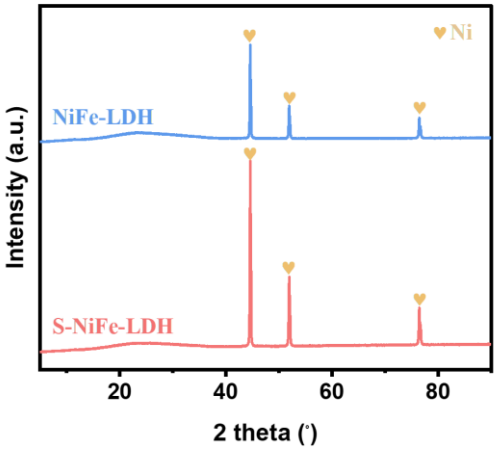

Fig. S2 XRD patterns of NiFe-LDH and S-NiFe-LDH.

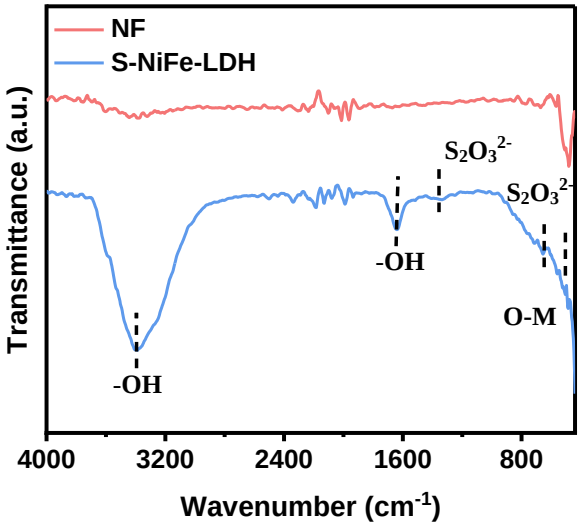

Fig. S3 FT-IR spectra of NF and S-NiFe-LDH.

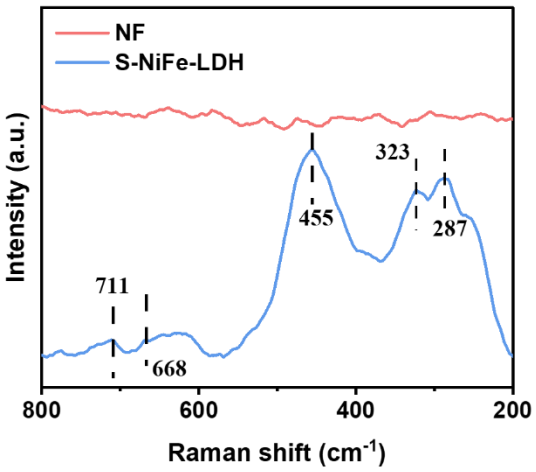

Fig. S4 Raman spectra of NF and S-NiFe-LDH.

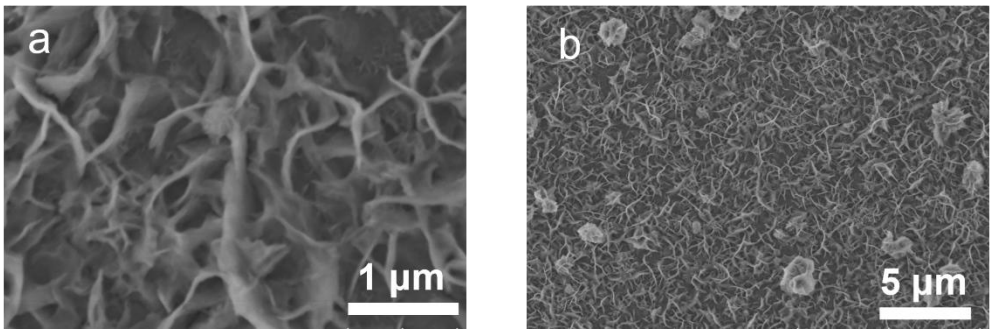

Fig. S5 (a, b) SEM images of NiFe-LDH.

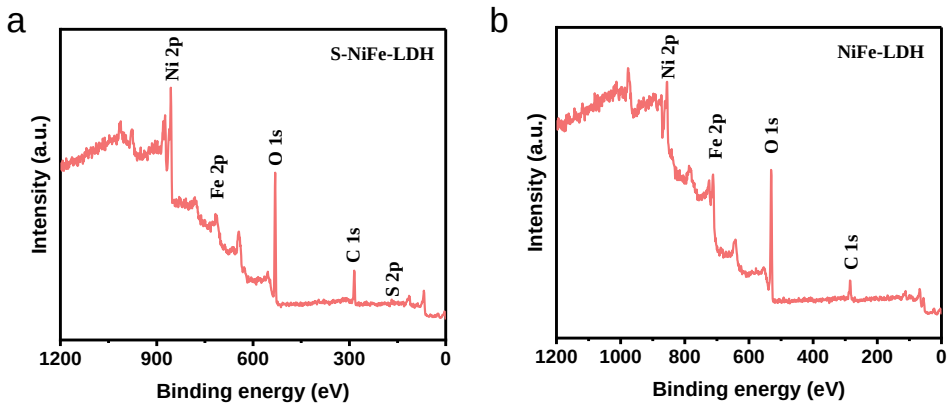

Fig. S6 XPS spectra of (a) S-NiFe-LDH and (b) NiFe-LDH.

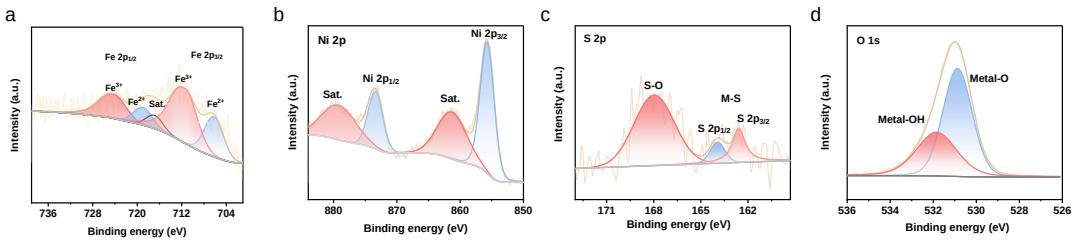

Fig. S7 High-resolution XPS spectra of (a) Fe 2p, (b) Ni 2p, (c) S 2p, and (d) O 1s for S-NiFe-LDH.

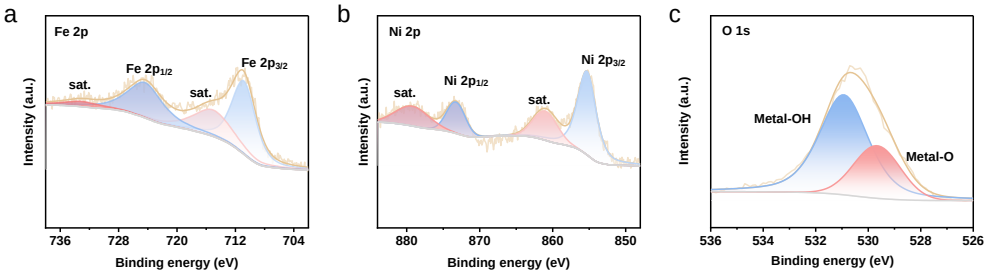

Fig. S8 High-resolution XPS spectra of (a) Fe 2p, (b) Ni 2p, and (c) O 1s for NiFe-LDH.

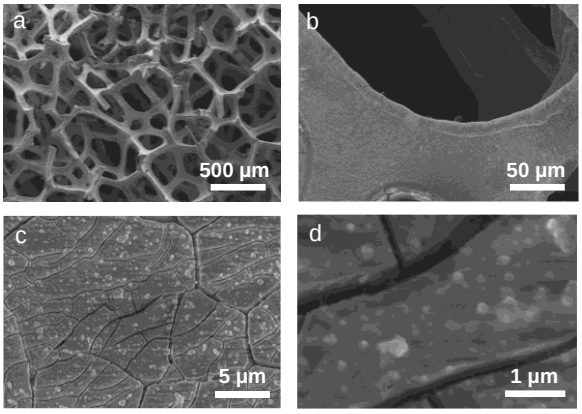

Fig. S9 (a-d) SEM images of S-NiFe-LDH.

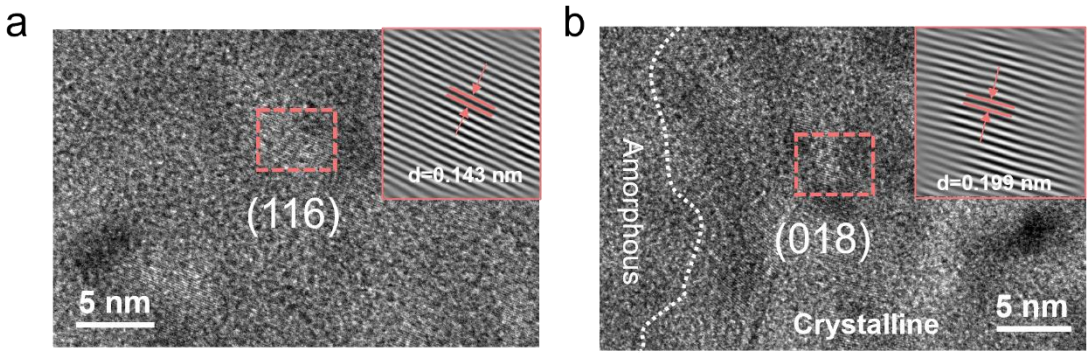

Fig. S10 (a, b) HRTEM images of NiFe-LDH.

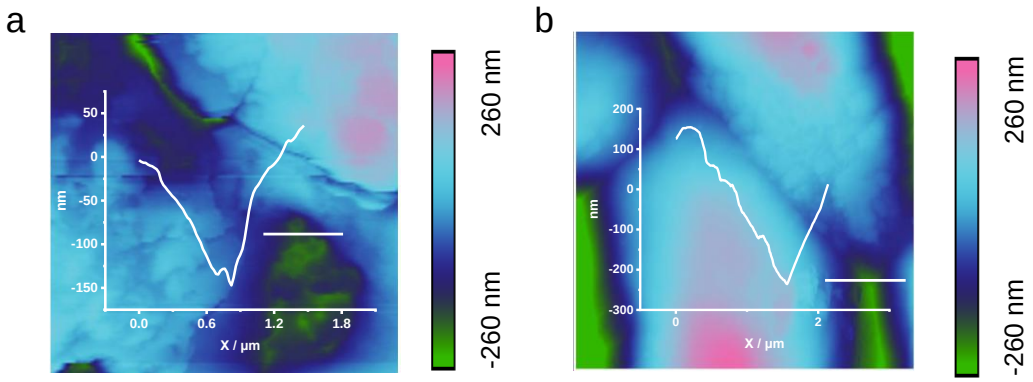

Fig. S11 AFM images of S-NiFe-LDH (a) before and (b) after the UOR stability test.

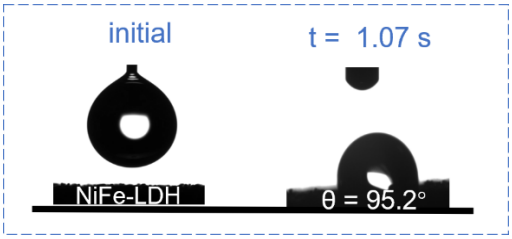

Fig. S12 The images of the droplet contact angles on the NiFe-LDH.

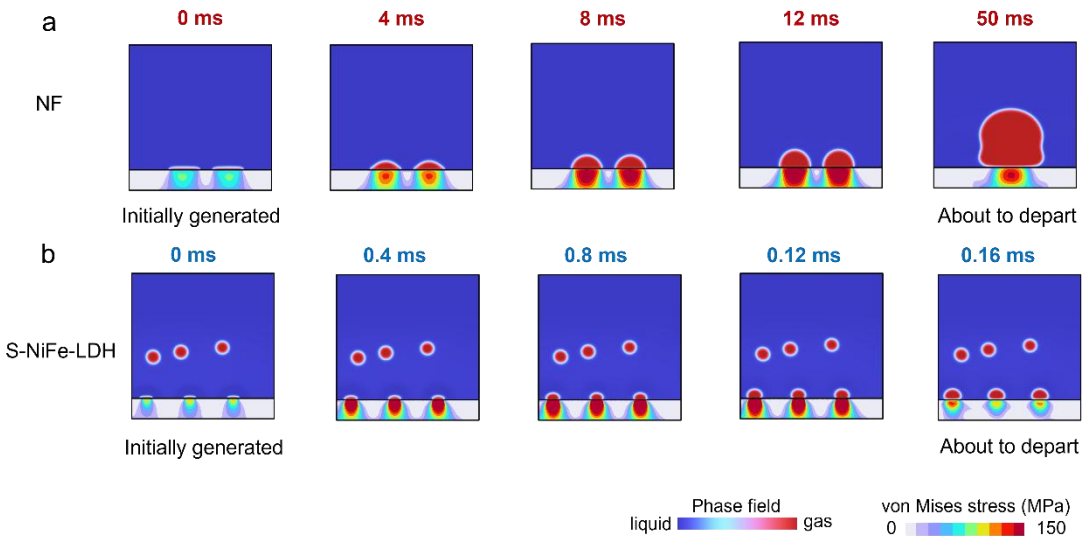

Fig. S13 Bubble evolution during UOR on (a) NF and (b) S-NiFe-LDH from nucleation to detachment by COMSOL simulation.

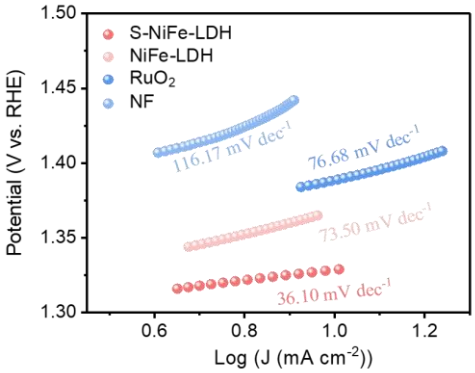

Fig. S14 Tafel plots measurements for UOR in 1 M KOH solution with 0.33 M urea.

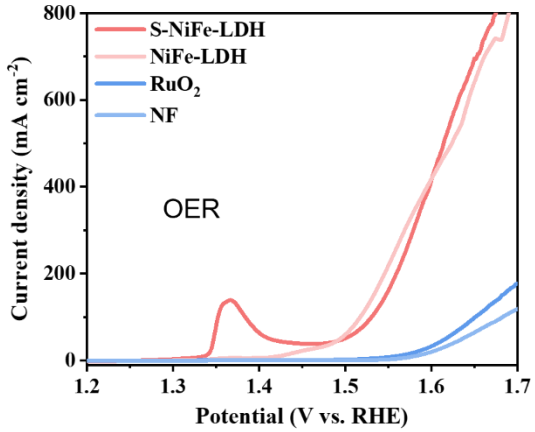

Fig. S15 Linear sweep voltammetry (LSV) curves (with *iR* compensation) for OER in 1 M KOH solution.

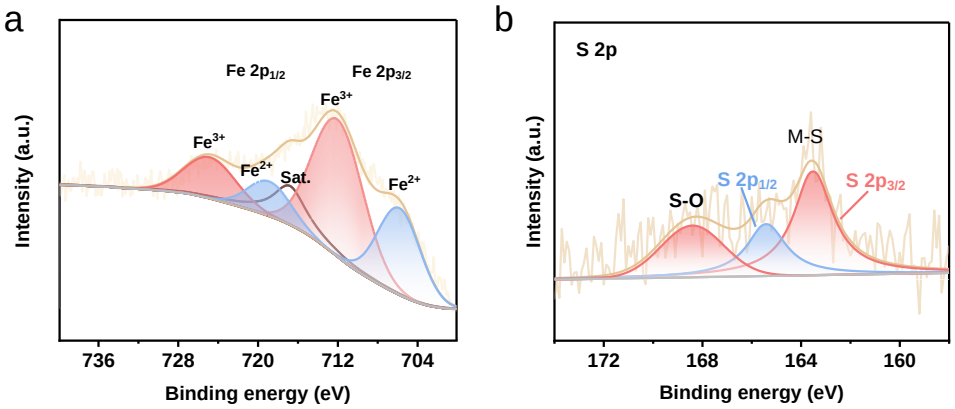

Fig. S16 High-resolution XPS spectra of (a) Fe 2p and (b) S 2p after UOR stability test for S-NiFe-LDH.

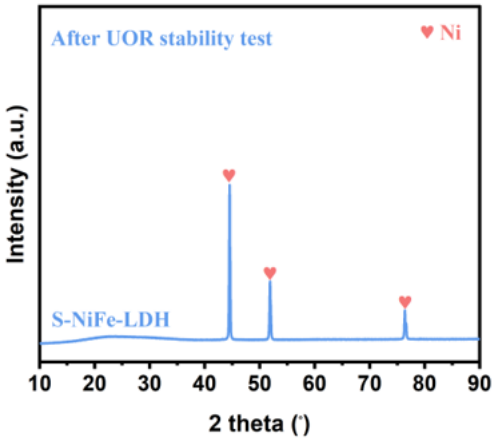

Fig. S17 XRD pattern of S-NiFe-LDH after UOR stability test.

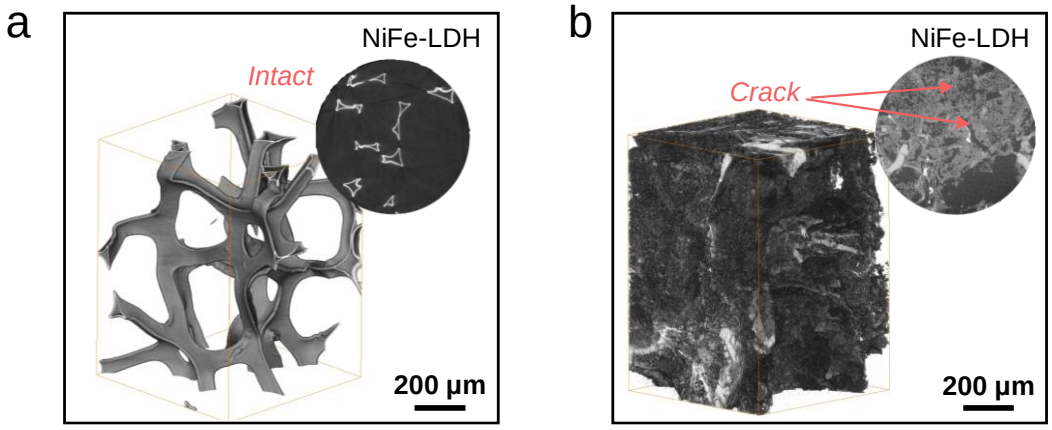

Fig. S18 (a) before and (b) after 360 h UOR stability test for NiFe-LDH.

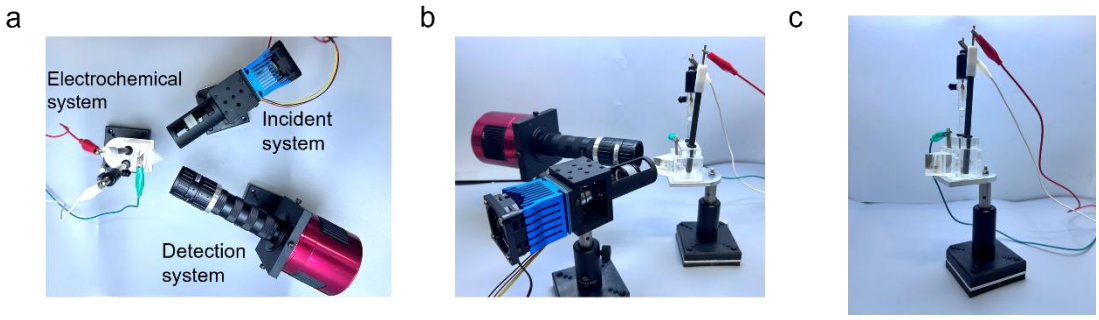

Fig. S19 In-situ TIR imaging setup. (a, b) Photographic images of the in-situ TIR system. (c) The electrochemical cell module with holder.

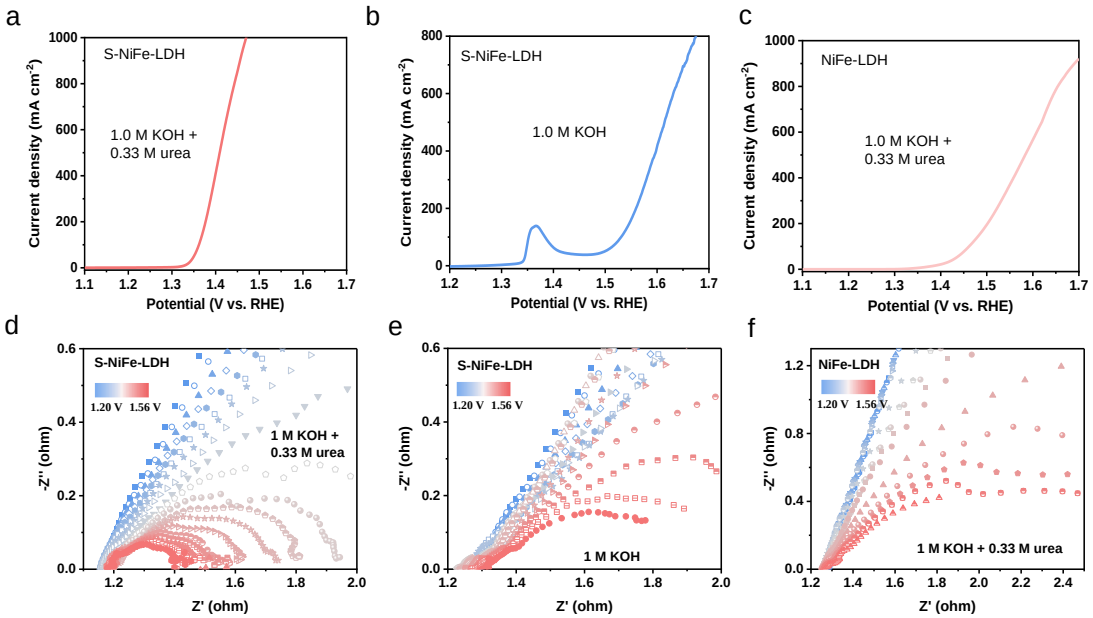

Fig. S20 (a) LSV curves (with *iR* compensation) of S- NiFe-LDH for UOR in 1 M KOH solution with 0.33 M urea; (b) LSV curves (with *iR* compensation) of S-NiFe-LDH for OER in 1 M KOH solution; (c) LSV curves (with *iR* compensation) of NiFe-LDH for UOR in 1 M KOH solution with 0.33 M urea; EIS Nyquist plots from 1.20-1.56 V of (d) S-NiFe-LDH in 1 M KOH solution with 0.33 M urea, (e) S-NiFe-LDH in 1 M KOH solution, and (f) S-NiFe-LDH in 1 M KOH solution with 0.33 M urea.

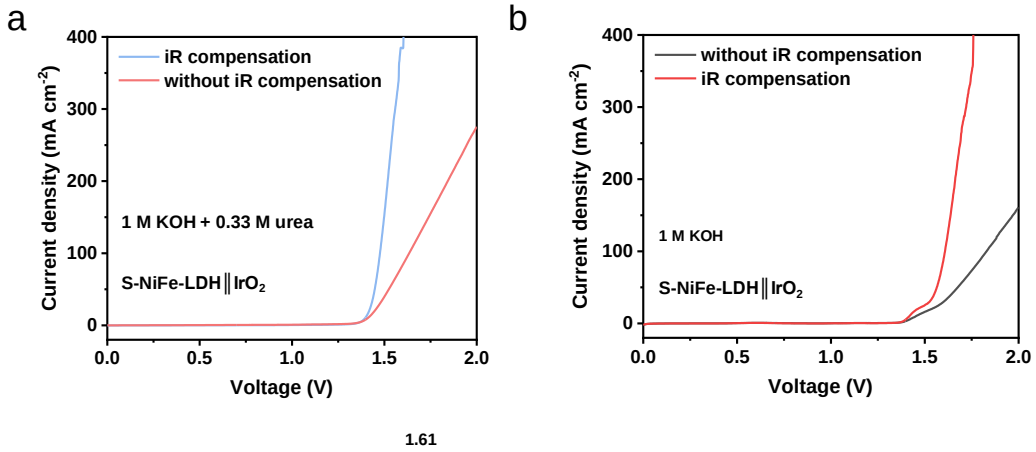

Fig. S21 LSV curves (with and without *iR* compensation) for (a) UAE in 1 M KOH with 0.33 M urea and (b) traditional AWE in 1 M KOH.

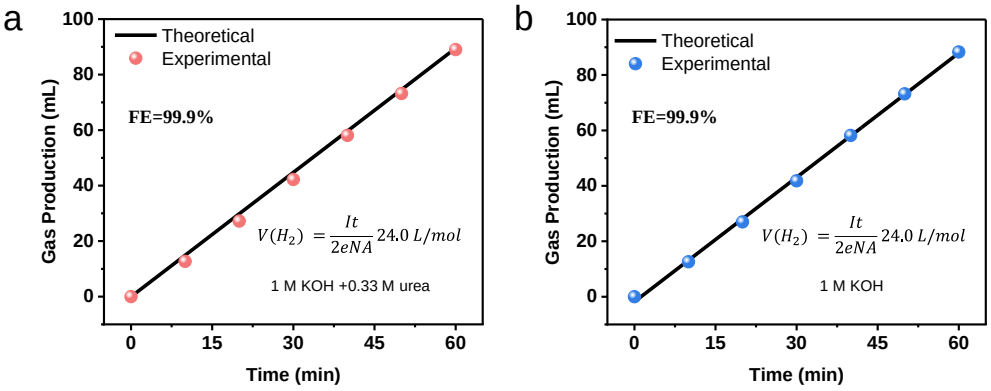

Fig. S22 Faradaic efficiency for hydrogen production of S-NiFe-LDH in (a) 1 M KOH solution with 0.33 M urea and (b) 1 M KOH solution.

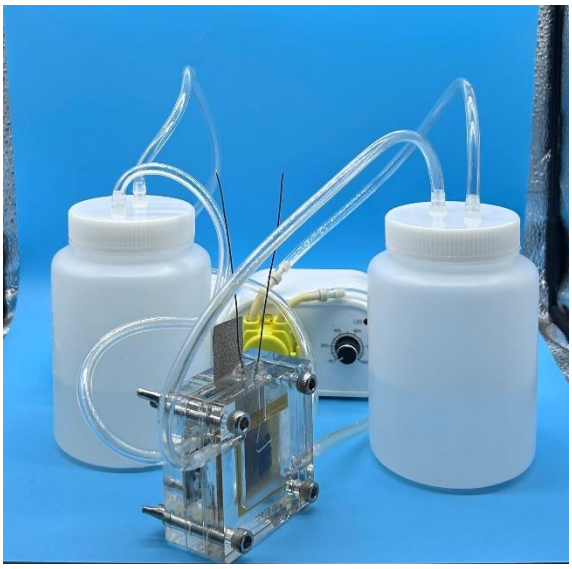

Fig. S23 Optical image of our home-made rechargeable three-electrode UOR-assisted zinc-air battery.

Table S1 Comparison of preparation time and catalysts stability for S-NiFe-LDH and other catalysts preparation methods used in the UOR.

Methods	Preparation time (h)	Stability time (h)	Catalysts	Ref.
one-step solution-phase	0.00056	360	S-NiFe-LDH	This work
coprecipitation	2	10	Ni-WO_x	[6]
electrospinning	4	50	Pt-$Ni(OH)_2$@Ni-CNF_{s-2}	[7]
hydrothermal	6.5	24	Mo-NiS/CFP	[8]
hydrothermal and anneal	8	50	NF/NiMoO-Ar	[9]
hydrothermal	11	60	$CoS_{1.097}/Ni_3S_2$	[10]

Table S2 Comparison of UOR performance (potential) of S-NiFe-LDH catalyst with reported UOR catalyst performance.

Catalysts	Potential (mV *vs.* RHE) at 100 mA cm^{-2}	Ref.
This work (S-NiFe-LDH)	1360	This work
Mo3-NT@NF	1442	[11]
FMC-n	1531	[12]
MoS_2 NPs/CoS_2 NTs	1504	[13]
P-CoS_2/Ti	1500	[14]
P-$CoS_x(OH)_y$NN/Ti	1571	[15]
S-NiMo/NF	1518	[16]
Ce-Ni_2P/NF	1473	[17]
Co-Z/Se-2	1443	[18]
$Ni_{1.5}Co_{1.5}$-O/CCs	1516	[19]
Ni-bza-900	1723	[20]

Table S3 Comparison of the S-NiFe-LDH assembled hybrid alkaline electrolyzer system with previously reported overall water splitting systems in cell performance.

Cell system	Electrolyte	Current density (mA cm^{-2})	Cell voltage (V)	Power consumption (kWh m^{-3} H_2)	Ref.
S-NiFe-LDH (+) || IrO_2 (–)	1.0 M KOH with 0.33 M urea	100	1.47	3.52	This work
CoMn/$CoMn_2O_4$ (+, –)	1 M KOH with 0.5 M urea	100	1.68	4.02	[21]
(Ru–Co)O_x (+, –)	1.0 M KOH	10	1.7	4.07	[22].
Ni-Mo nanotubes (+, –)	1 M KOH with 0.1 M urea	50	1.65	3.94	[23]
Co-Ni$(OH)_2$/CF (+, –)	1 M KOH with 0.5 M urea	75	1.72	4.11	[24]
NiNS/NF (+, –)	Seawater (+,–)	70	2.0	4.78	[25]
Ni_2P nanoflakes	1 M KOH with 0.5 M urea	50	1.78	4.25	[26]

Table S4 The operational cost breakdown of the UAE and AWE in the ideal scenario.

Parameters	UAE	AWE
Production rate (tones H_2/day)	10	10
Electrolyzer cost ($/kW)	450	450
Faradaic efficiency (%)	99.9	99.9
Capacity factor	0.8	0.8
Price ($ m^{-2})	10,000	10,000
Cell voltage (mV)	1470	1610
Current density (mA cm^{-2})	100	100
System lifetime (year)	20	20
Discount Rate (%)	7	7
Electrolyte lifetime (year)	1	1

* The input parameters are obtained from Ref.[27-31]

Supplementary Note. To determine the economic potential of hydrogen production from HSE, we carried out a simplified techno-economic analysis (TEA) based on a modified model.[27, 28, 30, 31] Table S5 summarizes all inputs used in the sample calculation with lab data conditions.

Below is the list of assumptions made for the calculations.

1. The production capacity of the plant is 10 tons of hydrogen per day.
2. The total catalyst and membrane cost is 5% of the electrolyzer cost.
3. The capacity factor is expected to be operational on any given day and is assumed to be 0.8, which means the plant will be operational 292 days a year.
4. The price of electricity is assumed to be $ 0.02 kWh^{-1}, taken from recent onshore wind power auctions.[29]
5. Capital cost includes the electrolyzer cost and catalyst and membrane cost.
6. The balance of the Plant is assumed to be 50% of the Capital cost.
7. Other operation and maintenance costs are assumed to be 10% of the Capital cost.
8. The faradaic efficiency for hydrogen generation is assumed to be 99.9%.
9. Due to the use of wastewater, the water consumption in the electrolyte is 0.

The calculation process

1. Electrolyzer cost

$$\text{Total electrolyzer cost} = \text{Power consumed} \times \frac{\text{base current density}}{\text{input current density}}$$

$$\text{Power consumed} = \text{Total current needed} \times \text{cell voltage}$$

$$\text{Total current needed} = \frac{\text{Plant capacity} \times \text{electrons transferred} \times \text{Faradaic constant}}{\text{Faradaic efficiency}}$$

$$\text{Capital recovery factor (CRF)} = \frac{\text{Discount rate} \times (1 + \text{Discount rate})^{\text{Lifetime}}}{(1 + \text{Discount rate})^{\text{Lifetime}-1}}$$

$$\text{Electrolyzer cost} = \frac{\text{Capital recovery factor} \times \text{Total electrolyzer cost}}{\text{Capacity factor} \times 365 \times \text{Plant capacity}}$$

2. Catalyst and membrane cost

$$\text{Catalyst and membrane cost} = \frac{\text{Capital recovery factor}_{C\&M} \times \text{Total electrolyzer cost} \times 5\%}{\text{Capacity factor} \times 365 \times \text{Plant capacity}}$$

3. Maintenance and Other operation costs

   Maintenance and Other operation costs = 10% × (Capital cost)

4. Balance of plant cost

   Balance of plant cost = 50% × (Capital cost)

5. Electricity cost

$$\text{Electricity cost} = \frac{Power\ consumed \times 24 \times \text{Electricity cost}}{\text{Plant capacity}}$$

Table S5 Comparison of average charging voltage between UOR-assisted Zinc-air battery assembled with S-NiFe-LDH and reported catalysts.

Current density (mA cm^{-2})	Average charging voltage (V)	Catalysts	Ref
100	2.00	S-NiFe-LDH	This work
5	2.15	FeCo@Co/N-C-8	[32]
5	2.20	SA-Ir/NC	[33]
8	2.02	FeCoNiMoW	[34]
10	2.25	0.05CoOx@PNC	[35]
10	2.33	Fe_3C@C-Fe SAS	[36]
50	2.09	CoFeNP@SA	[37]
100	2.24	$FeCoNiS_x$	[38]
10	2.17	FeMn-N-C	[39]

References

1. J. VandeVondele, M. Krack, F. Mohamed, M. Parrinello, T. Chassaing and J. Hutter, *Comput. Phys. Commun.*, 2005, **167**, 103-128.
2. T. D. Kühne, M. Iannuzzi, M. Del Ben, V. V. Rybkin, P. Seewald, F. Stein, T. Laino, R. Z. Khaliullin, O. Schütt, F. Schiffmann, D. Golze, J. Wilhelm, S. Chulkov, M. H. Bani-Hashemian, V. Weber, U. Borštnik, M. Taillefumier, A. S. Jakobovits, A. Lazzaro, H. Pabst, T. Müller, R. Schade, M. Guidon, S. Andermatt, N. Holmberg, G. K. Schenter, A. Hehn, A. Bussy, F. Belleflamme, G. Tabacchi, A. Glöß, M. Lass, I. Bethune, C. J. Mundy, C. Plessl, M. Watkins, J. VandeVondele, M. Krack and J. Hutter, *J. Chem. Phys.*, 2020, **152**, 194103.
3. J. P. Perdew, K. Burke and M. J. P. r. l. Ernzerhof, *Phys. Rev. Lett.*, 1996, **77**, 3865-3868.
4. Q. Hongxin, S. Xiaohao, W. Bozeng, S. Xinqian and H. Mingzhen, *Sci. Total Environ.*, 2024, **915**, 169969.
5. S. Grimme, J. Antony, S. Ehrlich and H. Krieg, *J. Chem. Phys.*, 2010, **132**, 154104.
6. L. Wang, Y. Zhu, Y. Wen, S. Li, C. Cui, F. Ni, Y. Liu, H. Lin, Y. Li, H. Peng and B. Zhang, *Angew. Chem. Int. Ed.*, 2021, **60**, 10577-10582.
7. M. Zhong, M. Xu, S. Ren, W. Li, C. Wang, M. Gao and X. Lu, *Energy Environ. Sci.*, 2024, **17**, 1984-1996.
8. Y. Zhou, Y. Wang, D. Kong, Q. Zhao, L. Zhao, J. Zhang, X. Chen, Y. Li, Y. Xu and C. Meng, *Adv. Funct. Mater.*, 2022, **33**, 2210656.
9. Z.-Y. Yu, C.-C. Lang, M.-R. Gao, Y. Chen, Q.-Q. Fu, Y. Duan, S.-H. J. E. Yu and E. Science, *Energy Environ. Sci.*, 2018, **11**, 1890-1897.
10. M. Du, Y. Ji, Y. Li, S. Liu and J. Yan, *Adv. Funct. Mater.*, 2024, 2402776.
11. M. Liu, W. Zou, J. Cong, N. Su, S. Qiu and L. Hou, *Small*, 2023, **19**, 2302698.
12. J. Jana, T. S. K. Sharma, J. S. Chung, W. M. Choi and S. H. Hur, *J. Alloys Compd.*, 2023, **946**, 169395.
13. T. L. Luyen Doan, D. C. Nguyen, K. Kang, A. Ponnusamy, H. I. Eya, N. Y. Dzade, C. S. Kim and C. H. Park, *Appl. Catal., B*, 2023, **342**, 123295.
14. Y. Jiang, S. Gao, J. Liu, G. Xu, Q. Jia, F. Chen and X. Song, *Nanoscale*, 2020, **12**, 11573-11581.
15. Y. Jiang, S. Gao, G. Xu and X. Song, *J. Mater. Chem. A*, 2021, **9**, 5664-5674.
16. J. Jiang, H. Jiang, M. Chen, R. Ma, X. Wang, W. Wei and L. Ai, *Appl. Surf. Sci.*, 2022, **600**, 154116.
17. K. Xiong, L. Yu, Y. Xiang, H. Zhang, J. Chen and Y. Gao, *J. Alloys Compd.*, 2022, **912**, 165234.
18. H. Xu, K. Ye, J. Yin, K. Zhu, J. Yan, G. Wang and D. Cao, *J. Power Sources*, 2021, **491**, 229592.
19. Y. Liu, J. Guan, W. Chen, Y. Wu, S. Li, X. Du and M. Zhang, *J. Alloys Compd.*, 2022, **891**, 161790.
20. J.-L. Liu, X.-Y. Zhou, J.-L. An, Y.-Q. Wang, M.-D. Zhang and L. Qin, *Energy Fuels*, 2022, **36**, 10346-10353.
21. C. Wang, H. Lu, Z. Mao, C. Yan, G. Shen and X. Wang, *Adv. Funct. Mater.*, 2020, **30**, 2000556.
22. C. Wang and L. Qi, *Angew. Chem. Int. Ed.*, 2020, **59**, 17219-17224.
23. J.-Y. Zhang, T. He, M. Wang, R. Qi, Y. Yan, Z. Dong, H. Liu, H. Wang and B. Y. Xia, *Nano Energy*, 2019, **60**, 894-902.
24. C. B. Sun, M. W. Guo, S. S. Siwal and Q. B. Zhang, *J. Catal.*, 2020, **381**, 454-461.
25. Y. Zhao, B. Jin, A. Vasileff, Y. Jiao and S.-Z. Qiao, *J. Mater. Chem. A*, 2019, **7**, 8117-8121.
26. H. Liu, S. Zhu, Z. Cui, Z. Li, S. Wu and Y. Liang, *Nanoscale*, 2021, **13**, 1759-1769.
27. J. Sisler, S. Khan, A. H. Ip, M. W. Schreiber, S. A. Jaffer, E. R. Bobicki, C.-T. Dinh and E. H. Sargent, *ACS Energy Lett.*, 2021, **6**, 997-1002.
28. P. De Luna, C. Hahn, D. Higgins, S. A. Jaffer, T. F. Jaramillo and E. H. Sargent, *Science*, 2019, **364**,

eaav3506.
29. M. Jouny, W. Luc and F. Jiao, *Ind. Eng. Chem. Res.*, 2018, **57**, 2165-2177.
30. H. Zhou, Y. Ren, Z. Li, M. Xu, Y. Wang, R. Ge, X. Kong, L. Zheng and H. Duan, *Nat. Commun.*, 2021, **12**, 4679.
31. W. R. Leow, Y. Lum, A. Ozden, Y. Wang, D.-H. Nam, B. Chen, J. Wicks, T.-T. Zhuang, F. Li, D. Sinton and E. H. Sargent, *Science*, 2020, **368**, 1228-1233.
32. L. Song, J. Zhang, S. Sarkar, C. Zhao, Z. Wang, C. Huang, L. Yan and Y. Zhao, *Chem. Eng. J.*, 2022, **433**, 133686.
33. X. Luo, M. Yang, W. Song, Q. Fang, X. Wei, L. Jiao, W. Xu, Y. Kang, H. Wang, N. Wu, W. Gu, L. Zheng, L. Hu and C. Zhu, *Adv. Funct. Mater.*, 2021, **31**, 2101193.
34. R. He, L. Yang, Y. Zhang, D. Jiang, S. Lee, S. Horta, Z. Liang, X. Lu, A. Ostovari Moghaddam, J. Li, M. Ibáñez, Y. Xu, Y. Zhou and A. Cabot, *Adv. Mater.*, 2023, **35**, 2303719.
35. Y. Tan, W. Zhu, Z. Zhang, W. Wu, R. Chen, S. Mu, H. Lv and N. Cheng, *Nano Energy*, 2021, **83**, 105813.
36. X. Wei, S. Song, N. Wu, X. Luo, L. Zheng, L. Jiao, H. Wang, Q. Fang, L. Hu, W. Gu, W. Song and C. Zhu, *Nano Energy*, 2021, **84**, 105840.
37. Z. Xu, C. Jiao, Z. Shu, Y. Xia, S. Chen, S. Chen and H.-L. Wang, *Chem. Eng. J.*, 2024, **481**, 148798.
38. A. Wang, X. Zhang, S. Gao, C. Zhao, S. Kuang, S. Lu, J. Niu, G. Wang, W. Li, D. Chen, H. Zhang, X. Zhou, S. Zhang, B. Zhang and W. Wang, *Adv. Mater.*, 2022, **34**, 2204247.
39. C. Hu, G. Xing, W. Han, Y. Hao, C. Zhang, Y. Zhang, C. H. Kuo, H. Y. Chen, F. Hu, L. Li and S. Peng, *Adv. Mater.*, 2024, **36**, 2405763.